RSC Sustainability

ROYAL SOCIETY OF CHEMISTRY

PAPER

View Article Online
View Journal | View Issue

Check for updates

Cite this: *RSC Sustainability*, 2026, **4**, 355

Hierarchically structured MOF-on-MOF photocatalysts with engineered charge dynamics for sustainable green fuel generation

Priyanka Priyadarshini, Subrat Kumar Sahoo and Kulamani Parida *

The limited photocatalytic performance of individual metal–organic frameworks (MOFs) restricts their practical use. To address this, the integration of distinct MOFs into MOF-on-MOF heterostructures can create well-defined charge-transfer interfaces, significantly enhancing photocatalytic efficiency. Motivated by this, we investigated the *in situ* assembly of ZIF-67 with NH_2-MIL-125(Ti), resulting in a binary ZIF-67/NH_2-MIL-125(Ti) all-solid-state Z-scheme heterostructure. Comprehensive characterisation through PXRD, BET, FTIR, UV-Vis spectroscopy, contact angle analysis and electrochemical studies confirmed enhanced structural and optoelectronic properties. Elemental profiling was carried out by ICP-OES, CHNO evaluation, and EDX spectroscopy. The hybrid catalyst exhibited an impressive H_2O_2 formation efficiency of 1345 μmol g^{-1} h^{-1}, accompanied by a quantum yield of 3.64% under 400 nm irradiation, and also delivered a H_2 evolution output of 215 μmol h^{-1}, each showing a fourfold improvement compared to the individual pristine MOFs. The synergistic interaction between the well-designed MOF-on-MOF heterostructure and the Z-scheme charge transfer mechanism effectively minimised charge recombination, as evidenced by XPS, PL spectra, TRPL, and EIS analyses. Furthermore, free radical trapping experiments and ESR studies confirmed the critical role of $^{\bullet}O_2^-$ radicals in the photocatalytic formation of H_2O_2. This study provides valuable insights for developing advanced MOF-based heterojunction photocatalysts tailored for efficient solar-to-chemical energy conversion.

Received 17th July 2025
Accepted 15th November 2025

DOI: 10.1039/d5su00595g

rsc.li/rscsus

Open Access Article. Published on 20 November 2025. Downloaded on 4/7/2026 5:17:10 PM.
This article is licensed under a Creative Commons Attribution-NonCommercial 3.0 Unported Licence.

Sustainability spotlight

Water and energy sustainability are critical pillars of global ecological balance. This study focuses on the development of hierarchically structured MOF-on-MOF photocatalysts for the efficient generation of green fuels, specifically hydrogen (H_2) and hydrogen peroxide (H_2O_2), through solar-driven processes. By addressing the limitations of individual metal–organic frameworks (MOFs) and leveraging their synergistic integration, this work offers a sustainable pathway for clean energy production and environmental remediation. The research aligns with the following UN Sustainable Development Goals (SDGs): SDG 7 (Affordable and Clean Energy); SDG 6 (Clean Water and Sanitation); SDG 9 (Industry, Innovation, and Infrastructure); and SDG 13 (Climate Action). This work underscores the potential of MOF-based photocatalysts to address pressing energy and environmental challenges while advancing global sustainability objectives.

1. Introduction

Hydrogen peroxide (H_2O_2) has recently garnered significant interest as an environmentally benign oxidant, widely utilised across various sectors such as chemical synthesis, food processing, paper manufacturing, medical sterilisation, and wastewater treatment. Its high-water solubility and the production of water (H_2O) as the only byproduct make H_2O_2 a promising energy carrier for future applications.[1,2] Multiple approaches have been developed for H_2O_2 synthesis, including the anthraquinone process, alcohol oxidation, direct combination of oxygen and hydrogen gases, and electrochemical methods.[3,4] However, these conventional techniques often suffer from major drawbacks such as high energy demands, excessive solvent usage, and safety risks due to the explosive nature of H_2/O_2 gas mixtures. Consequently, the development of a green, energy-efficient, and safe method for H_2O_2 production is highly sought after.[5,6] In this context, H_2O_2 generation through photocatalytic routes has risen as a promising alternative, leveraging photocatalysts to drive the reaction within O_2-saturated water or alcohol environments when exposed to light.[7]

Following the groundbreaking discovery by Fujishima and Honda, who demonstrated the photolytic splitting of water over a TiO_2 semiconductor under photoirradiation, the concept of photocatalytic water splitting has garnered considerable

Centre for Nano Science and Nano Technology, S 'O' A (Deemed to be University), Bhubaneswar, Odisha, 751030, India. E-mail: kulamaniparida@soa.ac.in; paridakulamani@yahoo.com

© 2026 The Author(s). Published by the Royal Society of Chemistry

Open Access Article. Published on 20 November 2025. Downloaded on 4/7/2026 5:17:10 PM. This article is licensed under a Creative Commons Attribution-NonCommercial 3.0 Unported Licence.

interest as a potential solution to the global energy challenge.[8] This pioneering work laid the foundation for the development of sustainable hydrogen (H_2) production technologies.[9] As the world grapples with the urgent need to transition away from depleting fossil fuels, hydrogen has emerged as a clean and renewable energy carrier with immense promise.[10] Among the various renewable energy strategies, photocatalytic hydrogen evolution from water stands out due to its cost-effectiveness, environmental benignity, and relatively straightforward operational setup.[11] A broad spectrum of inorganic semiconductors, such as TiO_2,[12] quantum dots,[13] perovskites,[14] MoS_2,[15] layered double hydroxides (LDHs),[16] and graphitic carbon nitride-based photocatalysts,[17] have been extensively studied for their ability to drive H_2 and H_2O_2 production under solar irradiation. Despite these advances, the practical implementation of these materials remains hampered by intrinsic limitations, including wide band gaps that confine light absorption to the ultraviolet region and suboptimal reaction efficiency resulting from the scarcity of catalytically accessible and inefficient charge separation.[18]

The domain of photocatalytic H_2O_2 and H_2 production has progressively shifted focus toward inorganic–organic hybrid architectures, attributable to the synergistic integration of the distinct properties of the individual constituents into a unified hybrid system. Metal–organic frameworks (MOFs), ordered materials comprising metal centres coordinated with organic linkers, have emerged as highly promising candidates.[19–21] Their structural tunability, adaptable framework design, and remarkably large surface area render them well-suited for photocatalytic applications driven by visible-light illumination, greatly improving both performance and product specificity.[22–24] Notably, MOFs with semiconducting properties have exhibited significant promise in diverse photocatalytic applications, including H_2 evolution from water, N_2 reduction, and H_2O_2 production, thereby presenting a promising avenue for improving overall photocatalytic efficiency.[25,26]

Titanium-based MOFs offer photocatalytic performance on par with TiO_2, with the added advantage of structural tunability that allows extension of light absorption from the UV into the visible region.[27] One of the first titanium-based MOFs developed was MIL-125, which consists of titanium-oxo clusters coordinated with terephthalic acid (BDC) as the organic linker.[28] Replacing BDC with 2-aminoterephthalic acid (NH_2-BDC) results in NH_2-MIL-125(Ti), a structurally similar framework where the introduction of amino groups serves as chromophores. This substitution lowers the band gap, enabling enhanced absorption in the visible spectrum compared to the UV-limited absorption of MIL-125.[29] Despite this improvement, NH_2-MIL-125(Ti) still exhibits restricted visible-light absorption and relatively low catalytic efficiency. This is primarily because the amino functionalisation predominantly raises the energy level of the valence band, which is situated on the organic moiety, whereas the conduction band, governed by the Ti-oxo nodes, stays mostly unchanged.[30] To overcome this limitation and enhance the visible-light activity and photocatalytic efficiency of NH_2-MIL-125(Ti) for applications like H_2O_2 and H_2 production, researchers have proposed the incorporation of a secondary component. This approach aims to tune the Ti-oxo nodes and shift the conduction band edge to more favourable levels.[31,32]

Among various heterostructure engineering strategies, the MOF-on-MOF approach, where one MOF is grown atop another possessing good structural integrity and photocatalytic capability, has shown significant promise, particularly for applications in aqueous environments.[33] The intimate interfacial contact achieved in such architectures facilitates more efficient charge separation and carrier transport, thereby markedly enhancing photocatalytic performance. The integration of two or more MOFs has attracted considerable research interest, as MOF-on-MOF structures can preserve desirable features such as high surface area, porosity, and crystallinity, all of which contribute to superior catalytic activity.[34,35] For example, Jiang *et al. in situ* synthesised a MOF-74/MOF-274 hybrid directly on NiFe alloy foam (NFF), resulting in a MOF-(74 + 274)@NFF composite. This structure demonstrated outstanding oxygen evolution reaction (OER) activity, attributed to phase conjugation-induced electronic modulation and the cooperative effect of Ni–Fe multimetallic centres.[36] A recent study by Sepehrmansourie *et al.* introduced an advanced heterostructure where UiO-66 was grown on NH_2-MIL-125 and further modified with g-C_3N_4 nanosheets, creating a UiO-66/NH_2-MIL-125/g-C_3N_4 Z-scheme system. This design significantly enhanced the visible-light photocatalytic degradation of ofloxacin.[37] In a 2025 study, researchers developed an innovative dual S-scheme heterojunction by integrating $BiVO_4$ with NH_2-MIL-125(Ti) and NH_2-MIL-53(Fe), forming a MOF@MOF hybrid. This system demonstrated outstanding photoelectrochemical (PEC) performance in the removal and detoxification of diverse organic pollutants.[38] Despite growing interest in MOF-based photocatalysis, studies focusing on NH_2-MIL-125(Ti)/MOF heterojunctions for photocatalytic H_2O_2 and H_2 generation remain limited in the literature.

The selection of a secondary MOF to construct a heterojunction with NH_2-MIL-125(Ti) should be guided by its optoelectronic characteristics, particularly its light absorption capability. Since NH_2-MIL-125(Ti) primarily absorbs in the early visible region, it is advantageous to pair it with an MOF that exhibits extended visible-light absorption. ZIF-67, a robust Co-based MOF known for its strong absorption in the visible spectrum, emerges as a suitable candidate. Accordingly, binary hybrid composites of NH_2-MIL-125(Ti) with ZIF-67 were successfully prepared *via* a simple *in situ* growth method at room temperature. These demonstrated markedly improved photocatalytic efficiency for visible-light-driven production of H_2O_2 and H_2, surpassing that of the individual parent MOFs. The observed improvement in photocatalytic efficiency is credited to superior light-harvesting ability, more enhanced separation of photogenerated charge carriers, and accelerated charge migration, as confirmed by UV-vis DRS, PL spectra, LSV study, TPC response, and EIS plots.

Additionally, the investigation explores the underlying reaction mechanism of O_2 photoreduction to H_2O_2 through tracer experiments. The results underscore the cooperative interaction involving NH_2-MIL-125(Ti) and ZIF-67 within the binary hybrid,

© 2026 The Author(s). Published by the Royal Society of Chemistry

Open Access Article. Published on 20 November 2025. Downloaded on 4/7/2026 5:17:10 PM.
This article is licensed under a Creative Commons Attribution-NonCommercial 3.0 Unported Licence.

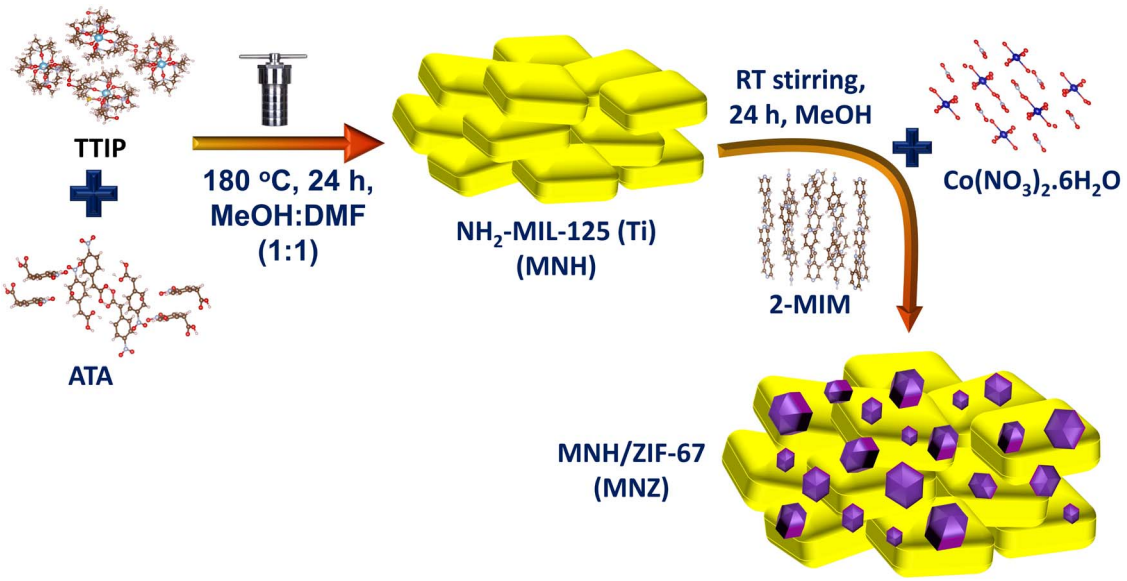

Scheme 1 Schematic illustration of the synthesis route for NH_2-MIL-125(Ti)/ZIF-67 (MNZ) binary hybrid.

which induces substantial modifications in their electronic and optical properties, ultimately boosting photocatalytic activity. Scheme 1 provides a schematic representation of the preparation pathway covering individual MOFs as well as their resulting composite, with detailed procedures outlined in the subsequent section.

2. Experimental section

2.1. Synthesis of NH_2-MIL-125(Ti) MOF

The amino-functionalized titanium-based MOF, NH_2-MIL-125(Ti) (denoted as MNH) was synthesised *via* a solvothermal approach. Specifically, 1.2 mL of titanium tetra-isopropoxide precursor (TTIP) and 0.53 g of 2-aminoterephthalic ligand were dissolved in a 1 : 1 mixture of DMF and methanol. The prepared reaction mixture was introduced into a 100 mL Teflon-lined stainless-steel autoclave, followed by thermal treatment at 180 °C for 24 h. Upon cooling, the yellow solid was separated *via* centrifugation and thoroughly washed multiple times using a methanol–DMF blend. The product was then vacuum-dried overnight at 80 °C, resulting in the formation of a bright yellow, amino-functionalized MIL-125(Ti) powder (MNH).

2.2. Synthesis of ZIF-67 MOF

ZIF-67 was synthesised through a simple stirring method at room temperature. First, 1.048 g of $Co(NO_3)_2 \cdot 6H_2O$ was dissolved in 50 mL of methanol to form a homogeneous solution A. Separately, 0.791 g of 2-methylimidazole was dispersed in another 50 mL of methanol to prepare solution B. A dropwise addition of solution B into solution A was performed under persistent stirring. The resulting mixture was allowed to react for 12 h at room temperature. The purple precipitate formed was separated *via* centrifugation, washed multiple times using methanol, and subsequently vacuum-dried to obtain pure ZIF-67 powder.

2.3. Synthesis of NH_2-MIL-125/ZIF-67 binary composites

For the fabrication of the NH_2-MIL-125(Ti) and ZIF-67 hybrid composite (MNZ), a precise quantity of NH_2-MIL-125 was uniformly dispersed in 50 mL of methanol containing 1.05 g of cobalt nitrate hexahydrate [$Co(NO_3)_2 \cdot 6H_2O$], referred to as mixture 1. The resulting solution underwent ultrasonication for 30 minutes, followed by magnetic stirring for an additional hour. Separately, 0.76 g of 2-methylimidazole was introduced and completely solubilized in methanolic solvent under ambient conditions to prepare mixture 2, which was quickly introduced into mixture 1 under stirring, and the resulting solution was kept under continuous stirring for 24 h. The resulting hybrid material was collected through centrifugation, washed thoroughly with methanol in three cycles, and subsequently vacuum-dried at 60 °C for 12 h to obtain the MNZ composite.

3. Results and discussion

3.1. Structural and morphological characterisation

PXRD study was employed to inspect the crystallographic structure and phase purity of the synthesised MNH, ZIF-67, and their binary composite MNZ. As presented in Fig. 1(a), for NH_2-MIL-125(Ti), well-defined diffraction peaks were detected at 6.82°, 9.82°, 11.6°, 15.07°, 16.7°, 18°, 19.6°, 22.8°, 23.5°, 24°, 26.2°, and 29.8°, which are in good agreement with previously reported patterns for this MOF (JCPDS#7211159).[39–41] ZIF-67 displayed its characteristic peaks at 7.3°, 10.3°, 12.6°, 14.7°, 16.4°, 18.09°, 22.1°, 24.4°, 25.5°, 26.6°, and 29.5°, consistent with the previous works (JCPDS#621030).[42–44] The PXRD pattern of the MNZ composite revealed the presence of all major peaks

Open Access Article. Published on 20 November 2025. Downloaded on 4/7/2026 5:17:10 PM.
This article is licensed under a Creative Commons Attribution-NonCommercial 3.0 Unported Licence.

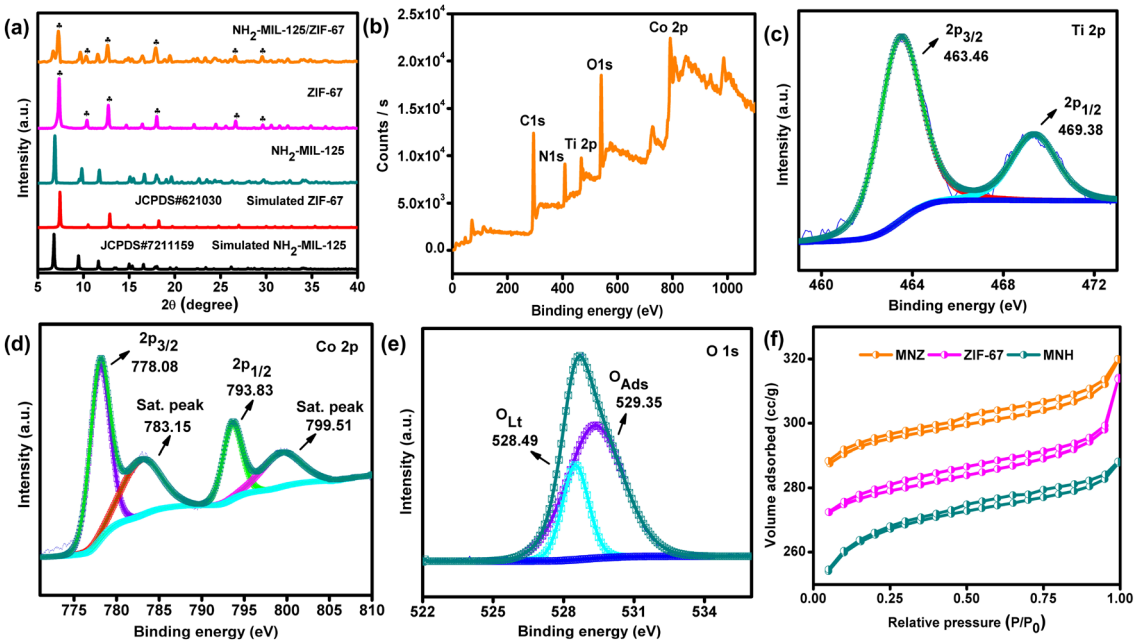

Fig. 1 (a) PXRD patterns of the synthesized photocatalysts. XPS spectra of MNZ: (b) survey scan, (c) Ti 2p, (d) Co 2p, (e) O 1s. (f) N_2 adsorption–desorption isotherms of the samples.

from MNH, as well as distinct peaks corresponding to ZIF-67. This confirms the successful formation of the composite without any notable loss in crystallinity, indicating that the structural integrity of both MOFs was well preserved upon integration. Scherrer's formula was utilised to estimate the crystallite dimensions of the synthesised materials, yielding values of 76.06 nm for MNH, 68.01 nm for ZIF-67, and 59.36 nm for the MNZ composite. The observed reduction in particle dimensions suggests improved material distribution and more robust interfacial connectivity between the MOF phases in the hybrid system. Furthermore, CHNO and ICP-OES analyses were conducted to determine the elemental composition of the binary MOF-on-MOF nanocomposite. The results confirmed the presence of C (39.90%), H (5.87%), N (11.67%), O (22.64%), Ti (10.01%), and Co (9.91%). These findings confirm the successful incorporation of Ti and Co from the respective parent MOFs, validating the formation of the hybrid structure and underscoring the existence of key elements essential for its photocatalytic functionality.

The FT-IR spectra displayed in Fig. S1 provide clear evidence of the successful synthesis and integration of MNH and ZIF-67 within the composite structure. For MNH, characteristic absorption bands are observed at 1600, 1500, 1440, and 1400 cm^{-1}, corresponding to the asymmetric and symmetric stretching vibrations of carbonyl groups. Moreover, the broad and intense absorption band observed around ~3405 cm^{-1} can be ascribed to the stretching vibrations of primary amine ($-NH_2$) groups in the organic linker, as well as to O–H stretching vibrations arising from adsorbed water molecules.[45,46] Meanwhile, the band appearing at 1625 cm^{-1} is associated with the N–H bending vibrations characteristic of aromatic amine groups.[47] A distinct absorption at 1250 cm^{-1} arises from benzene ring C–H bonds, while lower frequency modes (400–800 cm^{-1}) represent titanium-oxygen framework vibrations.[48,49] ZIF-67 is identified by its distinct peaks at 422, 1350, and 1500 cm^{-1}, associated with Co–N stretching and imidazole ring vibrations. Additional bands in the 900–1350 cm^{-1} and 500–800 cm^{-1} ranges correspond to in-plane and out-of-plane imidazole ring vibrations, respectively. A prominent peak at 1598 cm^{-1} is attributed to C=N stretching.[50] Consequently, the N–H stretching band in the MNZ appears to be slightly less intense and somewhat broader compared to MNH, probably because of minor changes in the hydrogen-bonding interactions or molecular environment of the amine groups upon composite formation. Except for this variation, the other characteristic bands of MNH and ZIF-67 have remained essentially unchanged, indicating that the structural frameworks of both the parent MOFs are well retained within the composite.

XPS analysis was conducted to investigate the elemental composition and chemical states of the photocatalysts. As shown in Fig. 1(b), the survey spectrum of the MNZ composite confirms the existence of Ti, Co, C, N, and O, aligning well with the results obtained from elemental mapping. In the case of MNH, the Ti 2p spectrum is deconvoluted into two distinct peaks at 462.10 eV (Ti $2p_{1/2}$) and 456.36 eV (Ti $2p_{3/2}$), indicative of Ti^{4+} species within the Ti-oxo clusters of the framework (Fig. S2(a)). In the MNZ hybrid material, the Ti 2p signals exhibit a slight positive shift, suggesting a net migration of electrons from MNH toward ZIF-67 upon heterostructure construction (Fig. 1(c)). The O 1s spectrum of MNH shows two primary peaks at approximately 527.7 eV and 529.3 eV, corresponding to lattice oxygen species (O_{Lt}, including O^{2-} in metal-oxo bonds) and surface-adsorbed oxygen (O_{Ads}), which may include O^-, O_2^-, or O_2^{2-} typically associated with surface hydroxyls (Fig. S2(c)). These spectral features are also present in the MNZ composite, with a slight positive shift, as illustrated in Fig. 1(e), further

© 2026 The Author(s). Published by the Royal Society of Chemistry

Open Access Article. Published on 20 November 2025. Downloaded on 4/7/2026 5:17:10 PM.
This article is licensed under a Creative Commons Attribution-NonCommercial 3.0 Unported Licence.

supporting the formation of strong interfacial interactions within the hybrid. The Co 2p XPS spectrum of the MNZ composite (Fig. 1(d)) displays two prominent peaks at 778.08 eV (Co $2p_{3/2}$) and 793.49 eV (Co $2p_{1/2}$), with a spin-orbit separation of approximately 15 eV. Additionally, broad satellite peaks at 783.19 eV and 799.39 eV, corresponding to Co $2p_{3/2}$ and Co $2p_{1/2}$, respectively, provide additional evidence for the effective integration of ZIF-67 into the composite. Compared to pristine ZIF-67 (Fig. S2(b)), these peaks exhibit a negative binding energy shift, suggesting charge transfer from the MNH framework to ZIF-67's surface. This shift strongly suggests that MNH functions as an electron donor upon hybridisation with ZIF-67. While determining the exact oxidation states of cobalt centres is often challenging, the binding energy gap spanning the main and satellite peaks provides critical insight: a gap of ~6.0 eV is indicative of Co(II), whereas Co(III) typically shows a larger separation of 9–10 eV.[51] Based on this criterion, the presence of Co(II) as the dominant oxidation state in the composite is evident. Altogether, these findings confirm effective interfacial charge transfer and support the operation of a bioinspired Z-scheme charge transfer mechanism within the hybrid system.

The porosity and textural characteristics of MNH, ZIF-67, and the MNZ composite were evaluated through nitrogen adsorption–desorption isotherm analysis. The linear BET plots for the photocatalysts, used to determine their corresponding surface areas, are shown in Fig. S3(a–c). Further details of the BET analysis are provided in the SI. Table S1 summarises the values corresponding to surface area, pore volume, and average pore size for the synthesised materials. As shown by the nitrogen adsorption–desorption analysis in Fig. 1(f), the parent MNH MOF followed a type IV isotherm accompanied by an H3 hysteresis loop, suggesting the presence of mesopores and the occurrence of capillary condensation at elevated relative pressures (P/P_0). Notably, MNH demonstrated a remarkably high specific surface area (S_{BET}) of 981.34 $m^2\ g^{-1}$, a feature that significantly enhances the accessibility of catalytic sites and thereby contributes to improved photocatalytic activity. The pristine ZIF-67 displayed a type II isotherm, which is typically associated with materials that are either non-porous or possess macroporous structures undergoing typical physical adsorption, with a notably high specific surface area (S_{BET}) of 1265.30 $m^2\ g^{-1}$. This substantial surface area is attributed to its 3D macroporous channel structure. The close consistency between measured and calculated S_{BET} (Table S1) further confirms the reliability of the surface area estimation for all three materials. Fig. S3(d) displays the pore distribution of the as-analysed photocatalysts. Upon forming the MNZ composite, the S_{BET} decreased to 759.78 $m^2\ g^{-1}$, and the isotherm exhibited features similar to the type IV isotherm and H3 hysteresis loop observed in MNH. This represents a 23% reduction in surface area and a 20% decrease in total pore volume. Such a reduction is considered moderate and is likely due to partial pore blockage by ZIF-67 within the composite framework, which restricts the internal porosity while simultaneously promoting structural rearrangements that facilitate the formation of mesopores. FESEM and HRTEM analyses further support this finding, revealing changes in the porosity and the development of mesostructured features (Fig. 2(a)–(c)). The presence of such mesopores is beneficial as they enhance the uptake of H_2O and O_2 species, thereby facilitating improved mass transport throughout the photocatalytic process.

Morphological and macrostructural features of the fabricated materials were investigated through scanning electron microscopy (SEM). As shown in Fig. S4(a), pure NH_2-MIL-125 exhibited a tablet-like morphology, with the surface appearing very smooth, aligning with previous reports.[39,52] The large surface area and functional framework of MNH offered a suitable platform for anchoring the dodecahedral ZIF-67. Following the growth of ZIF-67 onto the tablet-like MNH surface, the size, structure, and morphology of both MOFs were retained, confirming the structural stability of the MOF under various solvents and reductive environments (Fig. 2(a)). Elemental composition assessment *via* EDX for the MNZ nanocomposite confirms the presence of Ti along with Co, indicating the effective integration of ZIF-67 into MNH (Fig. S5). The obtained atomic weight% were 75.2% for C, 11.8% for O, 10.7% for N, 1.6% for Ti, and 0.7% for Co, as shown in Fig. S4(b) and (c). Moreover, no unexpected elements were detected, confirming the high purity of the synthesised nanocomposite. This further validates the formation of composite heterostructures, a feature that is anticipated to improve the effectiveness of photogenerated charge carrier separation and mobility. High-resolution transmission electron microscopy (HR-TEM) was utilised to further investigate the distribution of materials and the formation of heterojunctions between them. Detailed analysis was performed on the morphology and structural attributes of the synthesised samples. HR-TEM image of ZIF-67 displayed a uniform dodecahedral structure, which matches the existing literature (Fig. S6(a)).[53,54] Fig. 2(b) confirmed the growth of ZIF-67 microcrystals on the MNH surface, with deposition occurring both on the surface and along the edges. The results clearly demonstrate that dodecahedral ZIF-67 was firmly anchored to the cubic MNH, forming well-integrated NH_2-MIL-125(Ti)@ZIF-67 MOF-on-MOF binary hybrids. This close interfacial coupling is expected to promote efficient migration of photoinduced charge carriers during photocatalytic reactions. Fig. 2(c) presents the lattice fringes of MNH and ZIF-67, revealing distinct *d*-spacing values for each component. The MNH sample exhibited a *d*-spacing of 0.219 nm, corresponding to its characteristic lattice structure.[55] For ZIF-67, the measured *d*-spacing of 0.251 nm was assigned to the (111) lattice planes.[56] Particle size distribution analysis (Fig. 2(d)) indicated an average particle size of 150 nm. Although the S_{BET} of the MNZ composite showed a moderate decrease compared to the parent MOFs, this smaller particle size relative to the neat MOFs (Fig. S6(b) and (c)) enhances the material's external surface-to-volume ratio. This increase in exposed surface area, despite a slight reduction in total pore area, improves the accessibility of catalytically active sites and supports more efficient charge transport within the material. These findings align with the BET results, suggesting that while some internal pores may become partially blocked during composite formation, the overall external reactive surface remains more accessible for photocatalytic reactions.

Open Access Article. Published on 20 November 2025. Downloaded on 4/7/2026 5:17:10 PM.
This article is licensed under a Creative Commons Attribution-NonCommercial 3.0 Unported Licence.

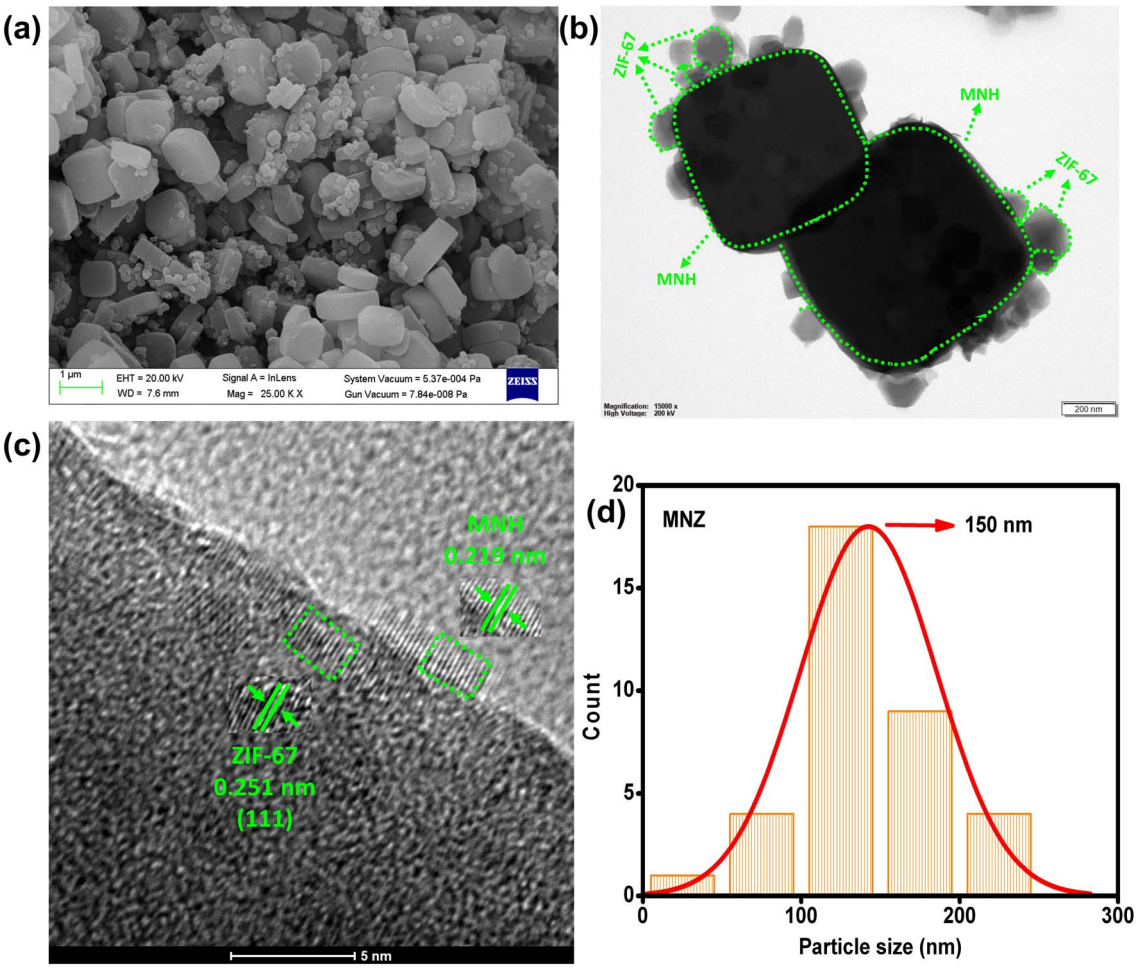

Fig. 2 (a) FESEM image of MNZ. (b) HRTEM image of MNZ. (c) Lattice fringe pattern of MNZ. (d) Particle size distribution of MNZ derived from HRTEM analysis.

3.2. Evaluation of photocatalytic activity

All synthesised photocatalysts were evaluated for H_2O_2 production through photoinduced oxygen reduction reactions using isopropyl alcohol as a hole scavenger under ambient temperature and pressure. The reactions were conducted in an environment pre-saturated with oxygen for two hours. As depicted in Fig. 3(a), the cumulative H_2O_2 production efficiency increased progressively from pristine MOFs to the MOF-on-MOF binary system. MNH exhibited limited H_2O_2 generation (677.0 μmol g^{-1} h^{-1}) under photoirradiation, primarily due to its limited light-harvesting capability within the visible region and rapid recombination of photoinduced charge carriers. Pristine ZIF-67 showed improved performance, producing 720 μmol g^{-1} h^{-1} of H_2O_2. However, the binary composite of MNH and ZIF-67 displayed a remarkable improvement in photocatalytic efficiency, attaining an H_2O_2 formation rate of 1345 μmol g^{-1} h^{-1}. This value was approximately fourfold greater than that of MNH and twice that of ZIF-67 under identical experimental conditions (Fig. 3(b)). The quantitative determination of H_2O_2 was based on the standard calibration curve shown in Fig. S7.

Contact angle measurements demonstrated that the binary MNZ composite exhibited a higher angle (105.3°) compared to neat MNH (88.4°), indicating enhanced surface hydrophobicity (Fig. S8(a) and (b)). This increased hydrophobicity promotes selective adsorption of non-polar O_2 molecules necessary for the reduction reaction while minimising excessive water adsorption that could lead to undesirable side reactions. Furthermore, the hydrophobic surface facilitates easier desorption of produced H_2O_2, thereby reducing its decomposition on the catalyst surface and improving product stability. The synergistic combination of ZIF-67-derived hydrophobicity with the redox-active NH_2-MIL-125(Ti) framework in MNZ substantially contributes to its superior H_2O_2 production efficiency relative to the individual MOF components.

Hydrogen peroxide (H_2O_2) is inherently unstable at room temperature, as it tends to decompose on the catalyst surface through interactions with photogenerated electrons and holes. Therefore, the overall amount of H_2O_2 produced is determined by the competing kinetics of its formation and decomposition. The final concentration is influenced by the interplay between the formation rate constant (K_f) and the decomposition rate constant (K_d), as described by eqn (1).[57]

© 2026 The Author(s). Published by the Royal Society of Chemistry

Open Access Article. Published on 20 November 2025. Downloaded on 4/7/2026 5:17:10 PM.
This article is licensed under a Creative Commons Attribution-NonCommercial 3.0 Unported Licence.

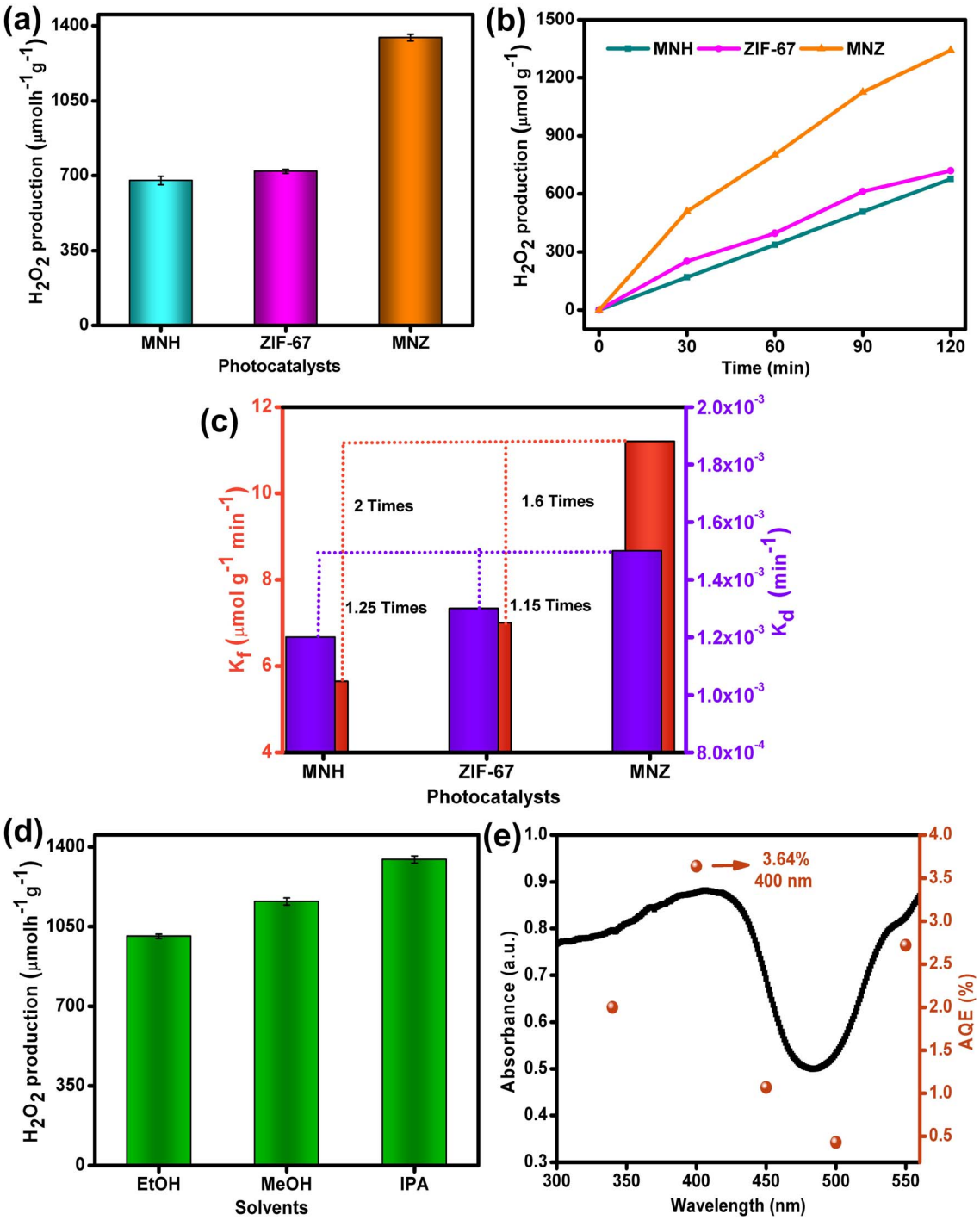

Fig. 3 (a) H_2O_2 production by the synthesised photocatalysts. (b) Time-dependent H_2O_2 generation. (c) Formation (K_f) and decomposition (K_d) profiles of H_2O_2. (d) H_2O_2 production using different sacrificial donors. (e) UV–vis absorption spectrum and AQE values of MNZ under various irradiation wavelengths. Error bars represent mean ± SD of three independent measurements.

$$[H_2O_2] = \frac{K_f}{K_d}\left(1 - e^{-K_d t}\right) \quad (1)$$

Here, t refers to the reaction time, and $[H_2O_2]$ indicates the concentration of hydrogen peroxide produced (μmol L^{-1}). The constants K_f and K_d denote the reaction rates for H_2O_2 formation (μmol L^{-1} min^{-1}) and its subsequent decomposition (min^{-1}), respectively. Moreover, C_t and C_0 denote the H_2O_2 concentration at time t and the initial concentration, respectively.

The H_2O_2 stability profile is illustrated in Fig. 3(c), beginning with an initial H_2O_2 concentration of 1000 μmol L^{-1} in the different catalytic systems under a N_2 atmosphere. Both the parent MOFs exhibited a deformation rate greater than the formation rate for H_2O_2. However, for the binary MOF

Open Access Article. Published on 20 November 2025. Downloaded on 4/7/2026 5:17:10 PM.
This article is licensed under a Creative Commons Attribution-NonCommercial 3.0 Unported Licence.

composite, MNZ, the formation rate was significantly higher than the deformation rate. Out of all the evaluated materials, the MNZ binary heterostructure demonstrated the highest efficiency in decomposing H_2O_2. This enhanced activity is ascribed to its improved spatial separation and directional migration of photoinduced charge carriers, allowing a greater number of charge carriers to effectively engage in the decomposition process. Accordingly, the kinetics of H_2O_2 formation and degradation were evaluated using a zero-order rate constant (K_f) to represent the formation process and a first-order rate constant (K_d) to describe the decomposition behaviour, as described by the kinetic model presented in eqn (2).[57]

$$K_d = \frac{-\ln(C_t/C_0)}{t} \quad (2)$$

As shown in Fig. 3(c), both parent MOFs exhibited relatively low K_f and K_d values, signifying restricted photocatalytic performance. In contrast, the MNZ composite exhibited a K_f value of 11.2 μmol g^{-1} min^{-1}, nearly fourfold and twofold greater than ZIF-67 and pristine MNH, respectively. Similarly, the K_d value for MNZ exceeded those of the individual MOFs, implying that simultaneous generation and breakdown of H_2O_2 were more pronounced in the presence of the composite catalyst. Nevertheless, the enhanced decomposition had a minimal effect on the overall H_2O_2 yield under light irradiation when using the binary photocatalyst. This confirms that the modification of ZIF-67 effectively enhances charge separation, allowing the rate of H_2O_2 formation to surpass its decomposition.

Additionally, various alcohols were introduced as electron donors into the reaction system, and their influence on the photocatalytic H_2O_2 production by MNZ was evaluated, as depicted in Fig. 3(d). The findings indicated that isopropanol was more effective in promoting H_2O_2 generation compared to ethanol and methanol. This is primarily attributed to the fact that an equal volume of isopropanol can release a higher amount of H^+ ions, which actively participate in the H_2O_2 formation process with MNZ. Consequently, the influence of varying concentrations of isopropanol on the photocatalytic performance of MNZ was further investigated and presented in Fig. S9(a). The results indicated that the H_2O_2 yield by MNZ increased with the rising amount of isopropanol. The highest H_2O_2 concentration was achieved at 2 mL of isopropanol, which can be considered the equilibrium point rate of the reaction and mass transport. Beyond this volume, an extra addition of isopropanol increased the viscosity of the reaction system, notably hindering oxygen diffusion and slowing down the reaction rate, ultimately causing a decrease in H_2O_2 concentration.

To assess the apparent quantum efficiency (AQE) for H_2O_2 generation, the performance of the MNZ photocatalyst was examined under different monochromatic light wavelengths employing appropriate band-pass filters ($\lambda_{band\text{-}pass}$ = 340, 400, 450, 500, and 550 nm), as shown in Fig. 3(e). Detailed AQE calculation procedures can be found in the SI. The highest AQE value of 3.64% was achieved at 400 nm, and progressively declines at longer wavelengths as reported in Table S2, which corresponds well with the light absorption spectrum.

To gain a deeper understanding of the photocatalytic H_2O_2 generation mechanism, a sequence of controlled experiments was designed and executed, as illustrated in Fig. S9(b). No significant H_2O_2 formation was observed in the absence of light, photocatalyst, or sacrificial agent, confirming their essential roles in the reaction. The significance of O_2 was further investigated by altering the reaction atmosphere. Fig. S9(b) shows H_2O_2 production under different conditions, including air, N_2, and O_2. Among these, the MNZ nanohybrid demonstrated the highest photocatalytic activity in an O_2-saturated environment, while negligible H_2O_2 generation was detected under air and N_2 atmospheres. These findings indicate that the photocatalytic process is highly dependent on the presence of dissolved O_2, which is crucial for H_2O_2 formation.

The influence of several individual parameters, including the initial pH of the reaction medium, the amount of MNZ composite photocatalyst, the type of electron donor, and the donor concentration, was systematically examined to evaluate their effects on the photocatalytic H_2O_2 production performance. As depicted in Fig. 4(a), the impact of initial pH ranging from 3 to 11 on H_2O_2 generation by MNZ was investigated. The highest H_2O_2 yield was obtained at neutral pH (pH = 7), while the production efficiency declined when the medium was either acidic or basic. This trend underscores how crucial interfacial charge dynamics, particularly electron and proton interactions, are in governing the photocatalyst's activity, which is sensitive to the pH of the reaction environment. Under acidic conditions, an excess of H^+ ions can interact with H_2O_2, resulting in its partial degradation. In contrast, under basic conditions, the presence of OH^- ions not only consumes H^+, thereby lowering the efficiency of H_2O_2 generation, but also accelerates the further decomposition of the formed H_2O_2. Moreover, extreme pH values such as 3 and 11 caused a significant drop in H_2O_2 generation. This reduction is primarily attributed to the structural instability of MNH in these conditions, wherein the terephthalate linkers undergo protonation, resulting in their dissociation from the $Ti_8O_8(OH)_4$ clusters, ultimately compromising the integrity of the MNH framework.

The quantity of photocatalyst plays a critical role in determining the efficiency of H_2O_2 production. As observed in Fig. S9(c), an upward trend in H_2O_2 production is seen with higher catalyst dosage, peaking at an optimal loading of 10 mg. This improvement is linked to the increased number of active sites available for oxygen adsorption, thereby enhancing the oxygen reduction reaction. However, further increase in the catalyst amount led to a decline in photocatalytic activity, primarily due to reduced light penetration and scattering effects, which limit effective light absorption and diminish overall efficiency. Moreover, the MNZ hybrid achieved a solar-to-chemical conversion efficiency (SCC%) of 0.025%, nearly twice that of MNH. The detailed calculation and the values are summarised in Table S3 as provided in the SI.

Reusability and stability are crucial parameters for evaluating the practical applicability of photocatalysts. In this study, the cyclic stability of MNZ was assessed through repeated photocatalytic experiments. Fig. 4(b) illustrates that the H_2O_2 production efficiency of MNZ declined by only 9% after four

© 2026 The Author(s). Published by the Royal Society of Chemistry

Open Access Article. Published on 20 November 2025. Downloaded on 4/7/2026 5:17:10 PM.
This article is licensed under a Creative Commons Attribution-NonCommercial 3.0 Unported Licence.

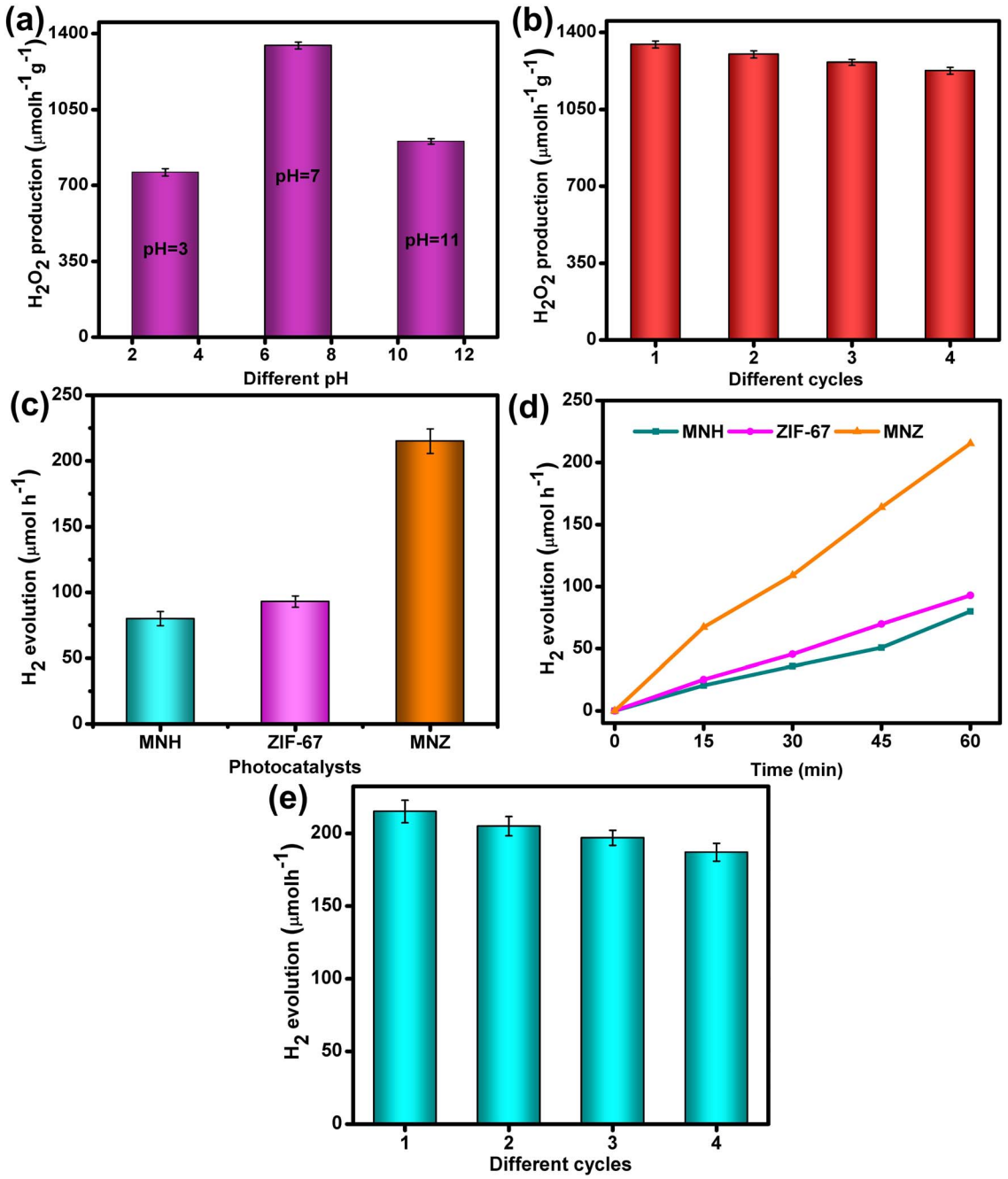

Fig. 4 (a) H_2O_2 production at different pH levels. (b) Reusability test of MNZ for H_2O_2 generation. (c) Photocatalytic H_2 evolution over all synthesised photocatalysts. (d) Time-dependent H_2 evolution profiles. (e) Reusability test of MNZ for H_2 evolution. Error bars represent mean ± SD of three independent measurements.

consecutive cycles, indicating excellent stability. Additionally, the FESEM, HRTEM, and PXRD analyses of MNZ after four cycles (Fig. S10) revealed no significant structural or morphological changes compared to the fresh sample, further confirming the durability and robustness of the photocatalyst for long-term application.

Beyond H_2O_2 generation, the catalyst's ability to drive photocatalytic hydrogen (H_2) evolution was assessed in the presence of a methanolic aqueous medium serving as a sacrificial hole scavenger under simulated visible-light irradiation ($\lambda \geq 400$ nm). Control tests demonstrated that hydrogen evolution did not take place when either the light source or the catalyst was excluded, confirming that both components are essential for efficient H_2 generation. For comparison, the photocatalytic H_2 evolution performances of MNH, ZIF-67, and the MNZ composite were investigated, as presented in Fig. 4(c). The hydrogen production of the pure photocatalysts exhibited a linear increase over time, indicating continuous H_2 generation under irradiation Fig. 4(d). Upon incorporation of ZIF-67, the hydrogen evolution rate of the composite significantly

Open Access Article. Published on 20 November 2025. Downloaded on 4/7/2026 5:17:10 PM. This article is licensed under a Creative Commons Attribution-NonCommercial 3.0 Unported Licence.

surpassed that of pristine MNH, demonstrating the enhanced photocatalytic output of the hybrid system. As displayed in Fig. 4(c), the MNZ composite exhibits an average photocatalytic evolution activity of 215 μmol h^{-1} under visible-light irradiation, approximately two and three times higher than that of ZIF-67 and MNH, respectively. This enhancement suggests that the incorporation of ZIF-67 into the composite framework effectively increases the number of surface-active sites, enhances the utilisation of photogenerated electrons, and suppresses electron–hole recombination, primarily because of the formation of numerous MNH/ZIF-67 interfacial junctions that generate new Co–N and Ti–O coordination centres, facilitating efficient charge transfer. Consequently, despite the slight reduction in S_{BET}, the interfacial synergy increases both the density and accessibility of catalytically active sites, leading to enhanced H_2 evolution performance. The calibration curve used for H_2 quantification is shown in Fig. S11. The apparent conversion efficiency (ACE) achieved for hydrogen evolution was measured to be 3.45%, nearly three times higher than that of pristine MNH. Detailed calculations and a table summary (Table S4) are provided in the SI. Beyond high H_2 evolution activity, reusability is also a vital criterion for an efficient photocatalyst. To assess this, the time-dependent hydrogen evolution performance of MNZ under visible light was tested over four cycles. As shown in Fig. 4(e), the H_2 production efficiency remained nearly unchanged, indicating the excellent stability and reusability of the MNZ photocatalyst.

3.3. Investigation of the enhanced catalytic activity

Motivated by the enhanced photocatalytic performance, a detailed investigation into the optical and electrochemical characteristics of the catalytic materials was conducted. The ability of a semiconductor to absorb visible light is a key factor influencing its photocatalytic efficiency. As illustrated in the UV–vis absorption profile (Fig. 5(a)), the MNH material displayed a strong optical response centred at 383 nm, suggesting limited responsiveness to visible light, with dominant absorption occurring in the near-ultraviolet range.[29] In contrast, ZIF-67 showed extended light uptake across the UV and visible regions, with significant absorption between 480–680 nm, primarily arising from the $^4A_2(F) \rightarrow {}^4T_1(P)$ electronic transition associated with Co^{2+} centres.[50] This observation confirms the predominance of tetrahedrally coordinated Co(II) centres within the ZIF-67 structure. The optical absorption edges for MNH and its ZIF-67 counterpart were observed at approximately 504 nm and 645 nm, corresponding to semiconductor band gaps of 2.46 eV (MNH) and 1.92 eV (ZIF-67). The binary heterostructure MNZ preserved the characteristic absorption features of its individual MOF constituents, with distinct signals corresponding to each framework, indicating that their electronic transitions remained intact. Moreover, a noticeable red shift in the absorption edge was observed for the MNZ composite, suggesting enhanced light absorption in the visible region. This improvement is primarily due to the incorporation of ZIF-67, which increases the absorption capacity, thereby promoting the formation of more photoinduced charge carriers during the catalytic process. The enhanced absorption is further supported by the visually darker appearance of ZIF-67, as evidenced in the UV–vis absorbance profile.

The optical band gap (E_g) is a crucial parameter for evaluating the potential of a material as an efficient photocatalyst. In this study, the E_g values were determined through Tauc plot extrapolation, by plotting $(\alpha h\nu)^{1/\gamma}$ *versus* photon energy ($h\nu$), following our previous study.[25,31] As demonstrated in Fig. S12(a)

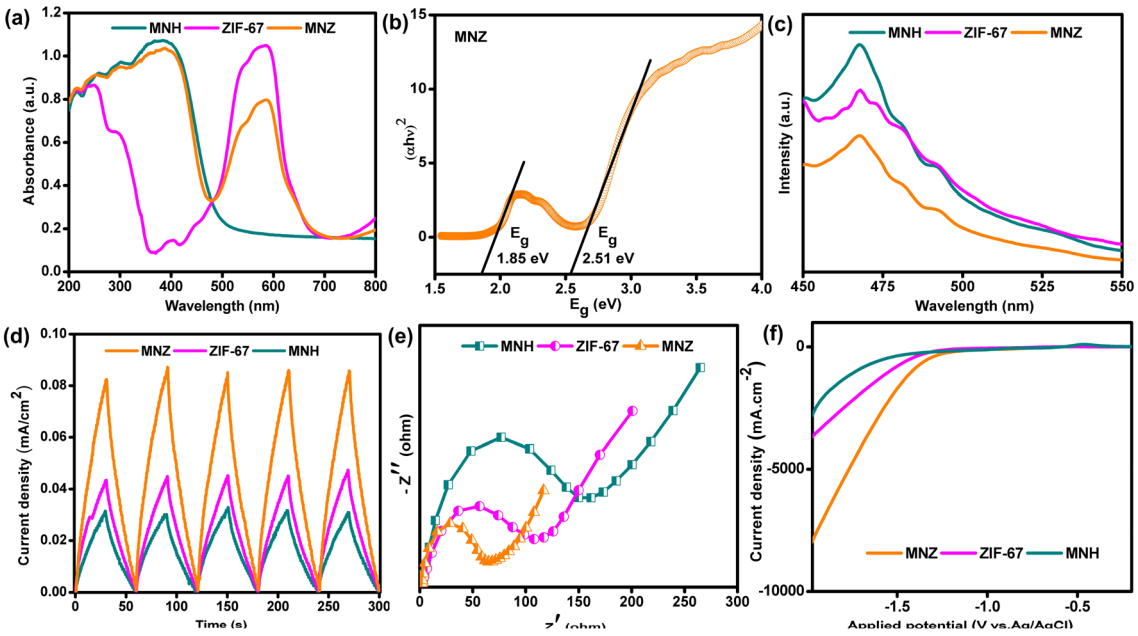

Fig. 5 (a) UV–vis DRS spectra of the synthesized samples. (b) Tauc plot for MNZ. (c) Steady-state PL spectra of the photocatalysts. (d) Transient photocurrent responses. (e) EIS Nyquist plots. (f) LSV curves of MNH, ZIF-67, and MNZ photocatalysts.

© 2026 The Author(s). Published by the Royal Society of Chemistry

Open Access Article. Published on 20 November 2025. Downloaded on 4/7/2026 5:17:10 PM.
This article is licensed under a Creative Commons Attribution-NonCommercial 3.0 Unported Licence.

and (b), the calculated band gaps were 2.53 eV for MNH and 1.95 eV for ZIF-67. For the binary MOF-on-MOF composite, two distinct band gap values were observed, with E_g values of 2.51 eV and 1.85 eV for the first and second transitions, respectively (Fig. 5(b)). These values are notably lower than the reported band gaps of pure ZIF-67 (1.98 eV) and MIL-125-NH_2 (2.65 eV), indicating enhanced visible light absorption. Analysis of the VB and CB potentials of MNH and ZIF-67 provides crucial insights into the photocatalytic H_2O_2 and H_2 production mechanism. Examination of the valence band XPS spectra (Fig. S12(c) and (d)) yielded VB potentials of 2.42 eV for MNH and 1.18 eV for ZIF-67. After getting the corresponding VB position, the CB values are calculated using eqn (3).

$$E_g = \mathrm{VB} - \mathrm{CB} \quad (3)$$

The as-obtained CB potentials were observed as −0.11 eV for MNH and −0.77 eV for ZIF-67. These energetically favourable band alignments between MNH and ZIF-67 enable the establishment of an efficient Z-scheme charge transfer pathway in the MNZ composite, which is critical for enhanced charge separation and photocatalytic performance. The flat band potentials determined through Mott–Schottky analysis (Fig. S12(e) and (f)) were −0.50 V for MNH and −1.26 V for ZIF-67 (*vs.* Ag/AgCl at pH = 7), with the positive slopes confirming their n-type semiconductor nature.

To further explore the separation behaviour of photogenerated charge carriers, steady-state photoluminescence (PL) spectra were recorded. PL analysis serves as a useful tool to assess the recombination efficiency of photoinduced excitons. As shown in Fig. 5(c), the pristine MNH displayed a strong emission peak centred at ∼468 nm when excited at 420 nm, indicating substantial electron–hole recombination. Under identical excitation, ZIF-67 also showed a distinct emission peak at ∼469 nm. Notably, the PL intensity for the MNZ composite was significantly quenched compared to both individual components. This considerable reduction in emission suggests that ZIF-67 incorporation into MNH effectively suppresses charge recombination by serving as a reservoir or mediator for charge carriers. The suppressed PL signal in MNZ confirms the presence of a well-established interfacial charge transfer pathway between MNH and ZIF-67, resulting in improved charge separation and accelerated surface reaction kinetics during photocatalysis. The transient photocurrent response under an on–off simulated light illumination was investigated to assess the charge separation behaviour of the photocatalysts. As presented in Fig. 5(d), MNH displayed the lowest photocurrent intensity, implying poor separation and mobility of photoinduced charge carriers. ZIF-67 also displayed a weak photocurrent, likely due to the insulating nature of its organic ligands, which tend to confine photogenerated electrons near the metal centres and hinder their transport. However, when ZIF-67 was integrated with MNH, the resulting MNZ composite showed a significantly enhanced photocurrent response. This improvement is attributed to the establishment of a heterojunction between MNH and ZIF-67, which effectively promotes efficient charge carrier separation and transfer, thereby enhancing photocatalytic efficiency. To further assess the electrical resistance and charge transfer dynamics, electrochemical impedance spectroscopy (EIS) was executed, as depicted in the corresponding Fig. 5(e). The characteristic arc observed in impedance spectra represents the interfacial resistance occurring at the material-electrolyte interface. A smaller semicircle indicates reduced resistance, implying improved charge separation efficiency. All samples exhibited clear semicircular profiles; however, the MNZ composite demonstrated the smallest arc radius among them. This suggests that MNZ possesses superior charge transport and migration abilities, facilitating more efficient surface reactions. Such enhanced conductivity contributes to better light harvesting and minimises the recombination of photogenerated carriers.

Furthermore, linear sweep voltammetry (LSV) measurements were employed to assess the photocurrent responses of the synthesized photocatalysts. As shown in Fig. 5(f), the cathodic photocurrent profiles of MNH, ZIF-67, and MNZ under visible-light illumination were compared. In alignment with earlier observations, ZIF-67 functions as an effective electron mediator, facilitating charge transport. As a result, the MNZ heterostructure displays a significantly elevated cathodic photocurrent. Notably, MNZ achieves a current density of −7861 mA cm^{-2}, which is approximately two and three times greater than that of the pristine ZIF-67 and MNH, respectively. This substantial enhancement in photocurrent suggests improved generation and transport of photoexcited electrons, attributed to effective charge carrier separation within the heterojunction. To further investigate the charge carrier dynamics, time-resolved photoluminescence (TRPL) measurements were conducted, as shown in Fig. S13(a). The pristine MNH exhibited an average emission lifetime of approximately ∼13 ns. In contrast, the binary MNZ composite showed a reduced average lifetime of 8.80 ns, while ZIF-67 alone displayed a lifetime of 9.11 ns. The noticeable quenching of PL intensity and shortened lifetime in MNZ indicate more rapid interfacial electron flow from MNH to ZIF-67 compared to the pristine MOF. These findings align well with previous TPC and EIS results, confirming effective separation of photoinduced exciton pairs and enhanced surface electron mobility in the MNZ system. Collectively, the strong interfacial coupling between MNH and ZIF-67 effectively suppresses charge recombination, accelerates electron transport, and reduces interfacial resistance, thereby improving overall photocatalytic performance.

To identify the primary reactive species involved in the photocatalytic generation of H_2O_2 using the MNZ photocatalyst under light exposure, radical scavenging experiments were performed, with the outcomes shown in Fig. S13(b). Several specific scavengers were employed to probe the role of different active species: 1,4-benzoquinone (PBQ) for superoxide radicals ($^{\bullet}O_2^-$), *tert*-butyl alcohol (TBA) for hydroxyl radicals ($^{\bullet}OH$), citric acid (CA) for photogenerated holes (h^+), and dimethyl sulfoxide (DMSO) for electrons (e^-). A marked decrease in H_2O_2 yield was observed upon the addition of PBQ and DMSO, suggesting that O_2^- and e^- play dominant roles in the photocatalytic process, likely through both direct and indirect O_2 reduction mechanisms. In contrast, the addition of TBA exerted negligible

Open Access Article. Published on 20 November 2025. Downloaded on 4/7/2026 5:17:10 PM. This article is licensed under a Creative Commons Attribution-NonCommercial 3.0 Unported Licence.

influence on H_2O_2 formation, implying $^{\bullet}OH$ species play only a minor role in this system. Conversely, the introduction of citric acid (CA) as a hole scavenger resulted in a significant enhancement in H_2O_2 generation. This improvement is ascribed to CA's ability to effectively scavenge photogenerated holes (h^+), thereby allowing a greater number of electrons to participate in the reduction of O_2. These observations indicate minimal involvement of h^+ and $^{\bullet}OH$ radicals in the H_2O_2 generation pathway. Importantly, the substantial suppression of H_2O_2 formation following the addition of either *p*-BQ or DMSO confirms that molecular oxygen reduction serves as the dominant route for H_2O_2 production. This supports a mechanism wherein H_2O_2 is formed primarily through a single-electron, two-step reduction process mediated by superoxide radicals ($^{\bullet}O_2^-$). Furthermore, when electrons were selectively scavenged, the MNZ system exhibited a 67% decline in H_2O_2 yield, underscoring the critical role of photogenerated electrons in driving the reaction. Furthermore, when PBQ was employed to scavenge superoxide radicals ($^{\bullet}O_2^-$), a notable reduction of 74% in H_2O_2 production was observed. This result indicates that the MNZ photocatalyst predominantly facilitates H_2O_2 generation through the reaction of photogenerated electrons with adsorbed O_2 molecules. It further confirms that the two-step, single-electron reduction mechanism is the dominant pathway for H_2O_2 production in the MNZ system. However, in addition to this primary mechanism, a minor contribution from the one-step, two-electron reduction of O_2, as well as limited oxidation of water by photogenerated holes, cannot be excluded. The involvement of reactive oxygen species was further corroborated by liquid-phase electron paramagnetic resonance (EPR) analysis using DMPO as a spin-trapping agent (Fig. S14). No signal corresponding to either $^{\bullet}OH$ or $^{\bullet}O_2^-$ radicals was detected under dark conditions, verifying that their formation is triggered by light exposure. Upon illumination with $\lambda > 420$ nm light, distinct signals corresponding to DMPO–$O_2^{\bullet-}$ and DMPO–$^{\bullet}OH$ adducts were observed for MNZ, confirming the light-induced generation of superoxide and hydroxyl radicals. These results highlight the enhanced formation of reactive species over MNZ due to efficient charge carrier separation and align well with the findings from the radical quenching tests.

3.4. Photocatalytic mechanism

In view of the comprehensive findings discussed earlier, the MNZ heterojunction demonstrated superior photocatalytic performance for both hydrogen and hydrogen peroxide generation when compared to the individual pristine photocatalysts. This improved efficiency primarily arises from its broadened light-harvesting capability across the visible spectrum and minimised charge carrier recombination, which stems from the effective establishment of a Z-scheme charge transport pathway. The proposed mechanism is illustrated in Scheme 2, which outlines the migration pathway of photogenerated exciton pairs in the MNZ system, thereby accounting for its remarkable photocatalytic properties. Based on the valence band XPS spectra data, the CB and VB energies of MNH were measured at −0.11 V and +2.42 V (*vs.* NHE), respectively. In comparison, ZIF-67 showed more negative CB (−0.77 V) and lower VB (+1.18 V) potentials. The band structures of the individual components confirm that both MNH and ZIF-67 can generate photogenerated electron–hole pairs under light irradiation, making them suitable candidates for constructing an efficient heterojunction photocatalyst. As depicted in Scheme 2, two plausible charge transfer pathways may be responsible for the improved photocatalytic activity of the MNZ heterostructure: (a) the dual charge transfer mechanism and (b) the Z-scheme charge transfer route. The proposed two-way charge migration involves electron flow from the lower-lying CB of ZIF-67 (−0.77 V) to the more positive CB level of MNH (−0.11 V). Simultaneously, photogenerated holes from the valence band (VB) of MNH (+2.42 V) would

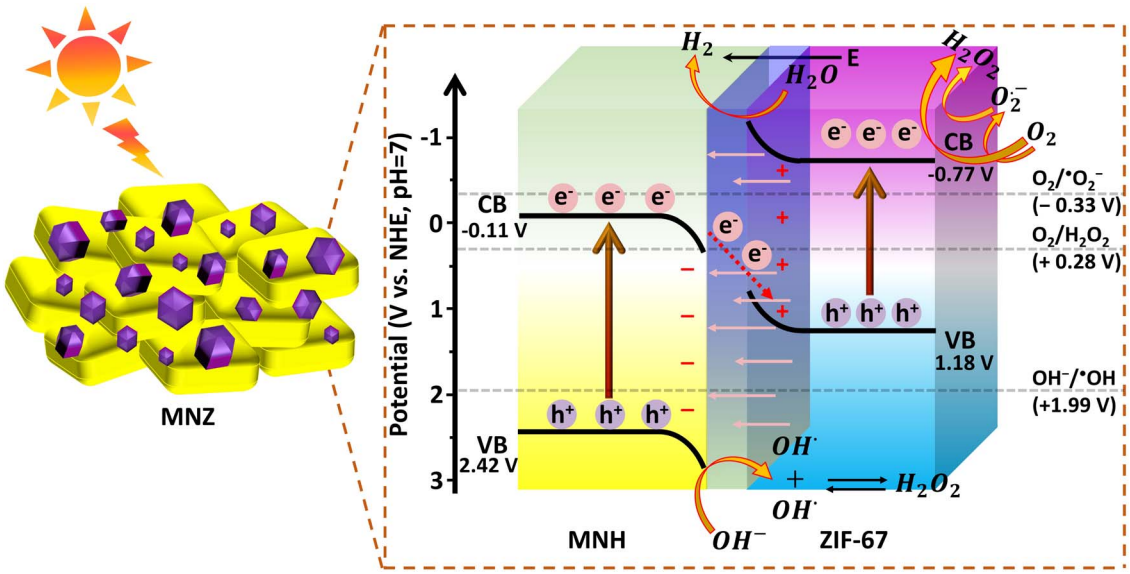

Scheme 2 Schematic representation of the proposed photocatalytic mechanisms for H_2O_2 and H_2 production over MNZ under light irradiation.

© 2026 The Author(s). Published by the Royal Society of Chemistry

Open Access Article. Published on 20 November 2025. Downloaded on 4/7/2026 5:17:10 PM. This article is licensed under a Creative Commons Attribution-NonCommercial 3.0 Unported Licence.

transfer to the VB of ZIF-67 (+1.18 V), owing to the potential difference. This leads to the accumulation of electrons in the CB of MNH, which are then available to reduce dissolved O_2, initiating the formation of superoxide radicals ($^{\bullet}O_2^-$) and subsequently promoting the generation of H_2O_2. However, as shown in Scheme 2, the VB position of ZIF-67 at +1.18 V is not sufficiently positive to facilitate the generation of hydroxyl radicals ($^{\bullet}OH$), since the redox potential required for $OH^-/^{\bullet}OH$ conversion is +1.99 V. This energy mismatch clearly indicates that the double charge transfer route is not energetically feasible and therefore cannot account for the improved photocatalytic performance of the MNZ heterostructure. As a result, the Z-scheme mechanism provides a more credible explanation. In this mechanism, under light exposure, photoexcited electrons within the CB of MNH migrate to the VB of ZIF-67, leading to recombination with holes and thus promoting spatial separation of the remaining charge carriers. Consequently, holes are retained in the VB of MNH (+2.42 V *vs.* NHE) while electrons accumulate in the CB of ZIF-67 (−0.77 V *vs.* NHE). This effective charge separation leads to improved photocatalytic activity. Moreover, the holes in the VB of ZIF-67 play a crucial role in oxidising IPA, facilitating proton generation and thereby increasing the electron concentration in ZIF-67's CB. As a result, this Z-scheme configuration maintains robust oxidation and reduction capabilities at the VB of MNH and CB of ZIF-67, respectively, consistent with the band structure deduced from XPS valence band measurements. Based on the proposed charge transfer dynamics, photoexcited electrons concentrate in the ZIF-67's CB, which is thermodynamically favoured at −0.77 V *vs.* NHE. This potential is sufficiently negative to fulfil the redox requirements of both the two-step single-electron pathway ($O_2 \rightarrow {}^{\bullet}O_2^- \rightarrow H_2O_2$) and the one-step two-electron pathway ($O_2 \rightarrow H_2O_2$), with redox potentials of −0.33 V and +0.28 V, respectively, thereby enabling efficient H_2O_2 generation under light irradiation.[58,59] Concurrently, the holes retained in the VB of MNH (+2.42 V) exhibit strong oxidative capability, exceeding the threshold potential of +1.99 V required for the $OH^-/^{\bullet}OH$ transformation, which can further react to form H_2O_2. The feasibility of this Z-scheme charge separation and migration is corroborated by XPS results, where a negative shift in ZIF-67's binding energy indicates increased donor density, confirming electron accumulation in its CB within the MNZ composite. Furthermore, the electron-rich CB of ZIF-67 is thermodynamically capable of reducing water to hydrogen gas. These mechanistic insights are strongly supported by the experimental outcomes of nitroblue tetrazolium (NBT) and terephthalic acid (TA) trapping experiments, aligning with the proposed photocatalytic charge transfer mechanism.

To confirm the proposed Z-scheme charge transfer mechanism between MNH and ZIF-67, we performed complementary radical trapping experiments using nitroblue tetrazolium (for $^{\bullet}O_2^-$ detection) and terephthalic acid (for $^{\bullet}OH$ quantification). The NBT assay was employed to detect the presence of superoxide radicals ($^{\bullet}O_2^-$), where a notable decrease in NBT concentration was observed for the MNZ heterostructure compared to the individual MOFs, as shown in Fig. S15(a). This confirmed the enhanced generation of $^{\bullet}O_2^-$ radicals in MNZ, indicating a more efficient electron transfer process. Additionally, the TA test was used to monitor hydroxyl radical ($^{\bullet}OH$) formation, identified by a characteristic photoluminescence emission peak at 425 nm. As depicted in Fig. S15(b), MNZ exhibited a significantly stronger PL intensity than pristine MNH or ZIF-67, signifying its superior ability to generate $^{\bullet}OH$ radicals during photocatalysis. Together, these findings strongly support the presence of a Z-scheme electron transfer mechanism in MNZ, wherein electrons are effectively shuttled to the ZIF-67 component of the binary heterostructure.

4. Conclusion

In summary, a binary MOF-on-MOF composite photocatalyst, NH_2-MIL-125/ZIF-67 (MNZ), was successfully fabricated *via* a simple *in situ* growth approach, achieving excellent photocatalytic performance for both H_2O_2 generation (1345 μmol g^{-1} h^{-1}) and H_2 evolution (215 μmol h^{-1}) under visible light with an AQE of 3.64%. The establishment of a heterojunction interface and the establishment of a Z-scheme charge transfer pathway within the MOF-on-MOF architecture significantly enhanced the separation efficiency of photogenerated charge carriers, thereby increasing the availability of electrons and holes for redox processes. This enhancement was corroborated by optoelectronic measurements, including suppressed steady-state PL emission, increased photocurrent response, and a smaller Nyquist arc radius, indicating efficient charge migration, stronger light harvesting, and improved O_2 adsorption. Moreover, ESR and radical scavenging experiments revealed that H_2O_2 was predominantly produced through a dual-step one-electron and a single-step two-electron reduction route. This study highlights the structural and functional merits of MOF-on-MOF heterojunctions and offers valuable insight into designing advanced MOF-based photocatalysts for energy and environmental applications.

Author contributions

Priyanka Priyadarshini: conceptualisation, methodology, investigation, formal analysis, validation, data curation, writing – original draft, review and editing. Subrat Kumar Sahoo: writing – review and editing, data curation, formal analysis. Kulamani Parida: conceptualisation, visualisation, writing – review and editing, supervision.

Conflicts of interest

There are no conflicts to declare.

Data availability

Data will be available on request.

Supplementary information: chemicals used; physicochemical characterization techniques; photoelectrochemical characterization procedures; photocatalytic H_2O_2 and H_2 production experiments; calculation of SCC%, AQE, and ACE%; XPS spectra of MNH; FTIR spectra; linear BET plots and pore size

Open Access Article. Published on 20 November 2025. Downloaded on 4/7/2026 5:17:10 PM. This article is licensed under a Creative Commons Attribution-NonCommercial 3.0 Unported Licence.

distribution curves of MNH, ZIF-67, and MNZ; FESEM image of MNH; EDX image of MNZ; HRTEM of ZIF-67 and histogram plots of MNH and ZIF-67; TRPL plots; Tauc plots of photocatalysts; XPS valence band spectra; Mott–Schottky plots; contact angle analysis; standard calibration curves of H_2O_2 and H_2; effect of IPA dosage, atmospheric conditions, and photocatalyst amount on H_2O_2 generation; UV–vis absorption spectra and AQE of MNZ; PXRD, FESEM, and HRTEM of MNZ post-photocatalysis; effect of scavengers on H_2O_2 production; TA and NBT assay plots; ESR spectra for superoxide and hydroxyl radicals. See DOI: https://doi.org/10.1039/d5su00595g.

Acknowledgements

The authors express their profound gratitude toward Siksha 'O' Anusandhan (Deemed to be University) for giving all the necessary facilities and financial support to carry out this immense research work.

References

1 B. O. Burek, J. Timm, D. W. Bahnemann and J. Z. Bloh, Kinetic effects and oxidation pathways of sacrificial electron donors on the example of the photocatalytic reduction of molecular oxygen to hydrogen peroxide over illuminated titanium dioxide, *Catal. Today*, 2019, **335**, 354–364, DOI: 10.1016/j.cattod.2018.12.044.

2 Y. Kondo, Y. Kuwahara, K. Mori and H. Yamashita, Design of metal-organic framework catalysts for photocatalytic hydrogen peroxide production, *Chem*, 2022, **8**, 2924–2938, DOI: 10.1016/j.chempr.2022.10.007.

3 A. Hayat, Z. Ajmal, A. Y. A. Alzahrani, S. Ben Moussa, M. Khered, N. Almuqati, A. Alshammari, Y. Al-Hadeethi, H. Ali and Y. Orooji, The photocatalytic H2O2 production: Design strategies, Photocatalyst advancements, environmental applications and future prospects, *Coord. Chem. Rev.*, 2025, **522**, 216218, DOI: 10.1016/j.ccr.2024.216218.

4 L. Zhu, W. Shi, H. Zhu, S. Feng and L. Wang, Breakthroughs in Photocatalytic Hydrogen Peroxide Production Through Advanced Mechanisms and Catalytic Systems, *Adv. Sustainable Syst.*, 2025, **9**, e00319, DOI: 10.1002/adsu.202500319.

5 S. Siahrostami, H_2O_2 electrosynthesis and emerging applications, challenges, and opportunities: A computational perspective, *Chem Catal.*, 2023, **3**, 100568, DOI: 10.1016/j.checat.2023.100568.

6 H. Chen, R. Chen, S. Liu, Y. Zhou, X. Chen, J. Cai, X. Lan, H. Jiang, L. Lin and Z. Sun, Efficient H2O2 Synthesis Through a Two-Electron Oxygen Reduction Reaction by Electrocatalysts, *Chempluschem*, 2024, **89**, e202400422, DOI: 10.1002/cplu.202400422.

7 S. Khan, M. A. Qaiser, W. A. Qureshi, S. N.-Z. Haider, X. Yu, W. Wang and Q. Liu, Photocatalytic hydrogen peroxide production: Advances, mechanistic insights, and emerging challenges, *J. Environ. Chem. Eng.*, 2024, **12**, 114143, DOI: 10.1016/j.jece.2024.114143.

8 K. Nakata and A. Fujishima, TiO2 photocatalysis: Design and applications, *J. Photochem. Photobiol., C*, 2012, **13**, 169–189, DOI: 10.1016/j.jphotochemrev.2012.06.001.

9 G. L. Chiarello, M. V Dozzi and E. Selli, TiO2-based materials for photocatalytic hydrogen production, *J. Energy Chem.*, 2017, **26**, 250–258, DOI: 10.1016/j.jechem.2017.02.005.

10 H. Nazir, C. Louis, S. Jose, J. Prakash, N. Muthuswamy, M. E. M. Buan, C. Flox, S. Chavan, X. Shi, P. Kauranen, T. Kallio, G. Maia, K. Tammeveski, N. Lymperopoulos, E. Carcadea, E. Veziroglu, A. Iranzo and A. M. Kannan, Is the H2 economy realizable in the foreseeable future? Part I: H2 production methods, *Int. J. Hydrogen Energy*, 2020, **45**, 13777–13788, DOI: 10.1016/j.ijhydene.2020.03.092.

11 S. Zhang, K. Wang, F. Li and S.-H. Ho, Structure-mechanism relationship for enhancing photocatalytic H2 production, *Int. J. Hydrogen Energy*, 2022, **47**, 37517–37530, DOI: 10.1016/j.ijhydene.2021.10.139.

12 R. Acharya and K. Parida, A review on TiO2/g-C3N4 visible-light- responsive photocatalysts for sustainable energy generation and environmental remediation, *J. Environ. Chem. Eng.*, 2020, **8**, 103896, DOI: 10.1016/j.jece.2020.103896.

13 J. Sahu, D. Prusty, S. Mansingh and K. Parida, A review on alloyed quantum dots and their applications as photocatalysts, *Int. J. Hydrogen Energy*, 2023, **48**, 29097–29118, DOI: 10.1016/j.ijhydene.2023.04.109.

14 A. Mishra, N. Priyadarshini, S. Mansingh and K. Parida, Recent advancement in LaFeO3-mediated systems towards photocatalytic and photoelectrocatalytic hydrogen evolution reaction: A comprehensive review, *Adv. Colloid Interface Sci.*, 2024, **333**, 103300, DOI: 10.1016/j.cis.2024.103300.

15 G. Swain, S. Sultana and K. Parida, A review on vertical and lateral heterostructures of semiconducting 2D-MoS2with other 2D materials: A feasible perspective for energy conversion, *Nanoscale*, 2021, **13**, 9908–9944, DOI: 10.1039/d1nr00931a.

16 L. Mohapatra and K. Parida, A review on the recent progress, challenges and perspective of layered double hydroxides as promising photocatalysts, *J. Mater. Chem. A*, 2016, **4**, 10744–10766, DOI: 10.1039/C6TA01668E.

17 S. K. Sahoo, L. Acharya, L. Biswal, P. Priyadarshini and K. Parida, Recent advancements in graphitic carbon nitride based direct Z- and S-scheme heterostructures for photocatalytic H2O2 production, *Inorg. Chem. Front.*, 2024, **11**, 4914–4973, DOI: 10.1039/d4qi00950a.

18 J. Low, J. Yu, M. Jaroniec, S. Wageh and A. A. Al-Ghamdi, Heterojunction Photocatalysts, *Adv. Mater.*, 2017, **29**, 1601694, DOI: 10.1002/adma.201601694.

19 P. Priyadarshini and K. Parida, Two-dimensional metal-organic frameworks and their derived materials: Properties, synthesis and application in supercapacitors field, *J. Energy Storage*, 2024, **87**, 111379, DOI: 10.1016/j.est.2024.111379.

20 N. Sultana, P. Priyadarshini and K. Parida, UiO-66-NH2 and its functional nanohybrids: unlocking photocatalytic potential for clean energy and environmental remediation,

© 2026 The Author(s). Published by the Royal Society of Chemistry

Open Access Article. Published on 20 November 2025. Downloaded on 4/7/2026 5:17:10 PM. This article is licensed under a Creative Commons Attribution-NonCommercial 3.0 Unported Licence.

Sustainable Energy Fuels, 2025, **9**, 3458–3494, DOI: 10.1039/d5se00150a.

21 P. Behera, P. Priyadarshini, J. Panda and K. Parida, Recent Advances in NH2-MIL-88B(Fe)-Based Photocatalysts for Environmental Remediation: Design Strategies, Mechanisms, and Applications, *Chem.–Asian J.*, 2025, **20**, e00541, DOI: 10.1002/asia.202500541.

22 D. Behera, P. Priyadarshini and K. Parida, ZIF-8 metal-organic frameworks and their hybrid materials: emerging photocatalysts for energy and environmental applications, *Dalton Trans.*, 2025, **54**, 2681–2708, DOI: 10.1039/d4dt02662d.

23 S. Subudhi, S. P. Tripathy and K. Parida, Highlights of the characterization techniques on inorganic, organic (COF) and hybrid (MOF) photocatalytic semiconductors, *Catal. Sci. Technol.*, 2021, **11**, 392–415, DOI: 10.1039/d0cy02034f.

24 S. Subudhi, S. P. Tripathy and K. Parida, Metal oxide integrated metal organic frameworks (MO@MOF): Rational design, fabrication strategy, characterization and emerging photocatalytic applications, *Inorg. Chem. Front.*, 2021, **8**, 1619–1636, DOI: 10.1039/d0qi01117g.

25 S. Subudhi, G. Swain, S. P. Tripathy and K. Parida, UiO-66-NH2 Metal–Organic Frameworks with Embedded MoS2 Nanoflakes for Visible-Light-Mediated H2 and O2 Evolution, *Inorg. Chem.*, 2020, **59**, 9824–9837, DOI: 10.1021/acs.inorgchem.0c01030.

26 S. Prakash Tripathy, S. Dash, A. Ray, S. Subudhi and K. Parida, Inexpensive Carbon Based Co-Catalyst Modified Zr-MOF Towards Photocatalytic H2O2 and H2 Production, *Chem.–Asian J.*, 2025, **20**, e202401115, DOI: 10.1002/asia.202401115.

27 X. Chen, X. Peng, L. Jiang, X. Yuan, H. Yu, H. Wang, J. Zhang and Q. Xia, Recent advances in titanium metal–organic frameworks and their derived materials: Features, fabrication, and photocatalytic applications, *Chem. Eng. J.*, 2020, **395**, 125080, DOI: 10.1016/j.cej.2020.125080.

28 K. Yue, X. Zhang, S. Jiang, J. Chen, Y. Yang, F. Bi and Y. Wang, Recent advances in strategies to modify MIL-125 (Ti) and its environmental applications, *J. Mol. Liq.*, 2021, **335**, 116108, DOI: 10.1016/j.molliq.2021.116108.

29 Y. Fu, D. Sun, Y. Chen, R. Huang, Z. Ding, X. Fu and Z. Li, An Amine-Functionalized Titanium Metal–Organic Framework Photocatalyst with Visible-Light-Induced Activity for CO2 Reduction, *Angew. Chem., Int. Ed.*, 2012, **51**, 3364–3367, DOI: 10.1002/anie.201108357.

30 P. Priyadarshini, A. Mishra, S. Nayak and K. Parida, NH2-MIL-125(Ti) and its functional nanomaterials - a versatile platform in the photocatalytic arena, *Nanoscale*, 2025, **17**, 4906–4957, DOI: 10.1039/d4nr03774j.

31 P. Priyadarshini, A. Mishra, A. Majhi, K. Parida and K. Parida, Engineering rGO-Driven Z-Scheme Charge Dynamics in NH2-MIL-125(Ti)/ZIF-67 for Superior Green Energy Applications, *ACS Appl. Energy Mater.*, 2025, **8**, 5067–5081, DOI: 10.1021/acsaem.4c03267.

32 T. Wu, X. Liu, Y. Liu, M. Cheng, Z. Liu, G. Zeng, B. Shao, Q. Liang, W. Zhang and Q. He, Application of QD-MOF composites for photocatalysis: Energy production and environmental remediation, *Coord. Chem. Rev.*, 2020, **403**, 213097, DOI: 10.1016/j.ccr.2019.213097.

33 L. Yuan, C. Zhang, Y. Zou, T. Bao, J. Wang, C. Tang, A. Du, C. Yu and C. Liu, A S-Scheme MOF-on-MOF Heterostructure, *Adv. Funct. Mater.*, 2023, **33**, 2214627, DOI: 10.1002/adfm.202214627.

34 C. Liu, J. Wang, J. Wan and C. Yu, MOF-on-MOF hybrids: Synthesis and applications, *Coord. Chem. Rev.*, 2021, **432**, 213743, DOI: 10.1016/j.ccr.2020.213743.

35 L. Chai, J. Pan, Y. Hu, J. Qian and M. Hong, Rational Design and Growth of MOF-on-MOF Heterostructures, *Small*, 2021, **17**, 2100607, DOI: 10.1002/smll.202100607.

36 Y. Jiang, T.-Y. Chen, J.-L. Chen, Y. Liu, X. Yuan, J. Yan, Q. Sun, Z. Xu, D. Zhang, X. Wang, C. Meng, X. Guo, L. Ren, L. Liu and R. Y.-Y. Lin, Heterostructured Bimetallic MOF-on-MOF Architectures for Efficient Oxygen Evolution Reaction, *Adv. Mater.*, 2024, **36**, 2306910, DOI: 10.1002/adma.202306910.

37 H. Sepehrmansourie, H. Alamgholiloo, N. Noroozi Pesyan and M. A. Zolfigol, A MOF-on-MOF strategy to construct double Z-scheme heterojunction for high-performance photocatalytic degradation, *Appl. Catal., B*, 2023, **321**, 122082, DOI: 10.1016/j.apcatb.2022.122082.

38 Q. Li, Q. Zhou, Y. Wu, Y. Shi, Y. Liu, H. Deng, S. Chen, Z. Li, E. Wang, H. Zhu and Q. Wang, Dual S-scheme heterojunction via MOF-on-MOF strategy for efficient photoelectrocatalytic removal of organic contaminants: Detoxification and mechanism, *J. Environ. Sci.*, 2025, **155**, 111–126, DOI: 10.1016/j.jes.2024.12.014.

39 T. Gao, H. Zhang, X. Zhao, S. Xiao, Z. Zhang and S. Yu, Efficient removal of tetracycline from MOF-on-MOF heterojunctions driven by visible light: Evaluation of photocatalytic mechanisms and degradation pathway, *Appl. Surf. Sci.*, 2024, **651**, 159227, DOI: 10.1016/j.apsusc.2023.159227.

40 S. Kuppusamy, D. Jagadeesan, A. M. Mohan, A. Pavoor Veedu, A. E. Jiji, A. M. John and P. Deivasigamani, NH2-MIL-125 MOF integrated translucent mesoporous polymer monolith as dual-light responsive new-generation photocatalyst for the expeditious decontamination of perennial pharmaceuticals, *J. Environ. Chem. Eng.*, 2023, **11**, 110355, DOI: 10.1016/j.jece.2023.110355.

41 A. K. Kar, A. Behera and R. Srivastava, Pd-Embedded Ti Metal–Organic Framework Nanostructures for Photocatalytic Reductive N-Formylation of Nitroarenes in Water, *ACS Appl. Nano Mater.*, 2022, **5**, 464–475, DOI: 10.1021/acsanm.1c03310.

42 H. Gong, X. Zhang, G. Wang, Y. Liu, Y. Li and Z. Jin, Dodecahedron ZIF-67 anchoring ZnCdS particles for photocatalytic hydrogen evolution, *Mol. Catal.*, 2020, **485**, 110832, DOI: 10.1016/j.mcat.2020.110832.

43 Y. Ke, J. Zhang, L. Liu, X. Li, Q. Liang and Z. Li, Self-Assembled Zeolitic Imidazolate Framework/CdS Hollow Microspheres with Efficient Charge Separation for Enhanced Photocatalytic Hydrogen Evolution, *Inorg. Chem.*, 2022, **61**, 10598–10608, DOI: 10.1021/acs.inorgchem.2c01697.

Open Access Article. Published on 20 November 2025. Downloaded on 4/7/2026 5:17:10 PM. This article is licensed under a Creative Commons Attribution-NonCommercial 3.0 Unported Licence.

44 A. Khamis, A. S. Mahmoud, A. O. A. El Naga, S. A. Shaban and N. A. Youssef, Activation of peroxymonosulfate with ZIF-67-derived Co/N-doped porous carbon nanocubes for the degradation of Congo red dye, *Sci. Rep.*, 2024, **14**, 12313, DOI: 10.1038/s41598-024-62029-8.

45 J. Zhou, Q. Jia, L. Gong, S. Zhang, X. Zhou and H. Song, Enhanced Z-scheme ZnS/NH2−MIL-125(Ti) photocatalysts with biomass-derived carbon quantum dots for CO2 reduction, *Mol. Catal.*, 2024, **552**, 113715, DOI: 10.1016/j.mcat.2023.113715.

46 D. Ao, J. Zhang and H. Liu, Visible-light-driven photocatalytic degradation of pollutants over Cu-doped NH2-MIL-125(Ti), *J. Photochem. Photobiol., A*, 2018, **364**, 524–533, DOI: 10.1016/j.jphotochem.2018.06.044.

47 S. Li, Y. Fang, J. Mu, X. Sun, H. He, Y. Cao and B. Liu, Photocatalytic removal of Cr(VI) and efficient degradation of tetracycline by oxygen-enriched vacancy pie-like NH2-MIL-125(Ti), *Colloids Surf., A*, 2024, **680**, 132734, DOI: 10.1016/j.colsurfa.2023.132734.

48 Y. Wu, X. Li, Q. Yang, D. Wang, F. Yao, J. Cao, Z. Chen, X. Huang, Y. Yang and X. Li, Mxene-modulated dual-heterojunction generation on a metal-organic framework (MOF) via surface constitution reconstruction for enhanced photocatalytic activity, *Chem. Eng. J.*, 2020, **390**, 124519, DOI: 10.1016/j.cej.2020.124519.

49 S. He, Q. Rong, H. Niu and Y. Cai, Platform for molecular-material dual regulation: A direct Z-scheme MOF/COF heterojunction with enhanced visible-light photocatalytic activity, *Appl. Catal., B*, 2019, **247**, 49–56, DOI: 10.1016/j.apcatb.2019.01.078.

50 H. Park, D. Amaranatha Reddy, Y. Kim, R. Ma, J. Choi, T. K. Kim and K.-S. Lee, Zeolitic imidazolate framework-67 (ZIF-67) rhombic dodecahedrons as full-spectrum light harvesting photocatalyst for environmental remediation, *Solid State Sci.*, 2016, **62**, 82–89, DOI: 10.1016/j.solidstatesciences.2016.10.018.

51 J. Wang, Y. Li, S. Xu, C. Lin, X. Ma, Y. Ni and S. Cao, Novel functionalization of ZIF-67 for an efficient broad-spectrum photocatalyst: formaldehyde degradation at room temperature, *New J. Chem.*, 2022, **46**, 2962–2970, DOI: 10.1039/D1NJ06192E.

52 X. Zheng, Y. Li, J. Yang and S. Cui, Z-Scheme heterojunction Ag/NH2-MIL-125(Ti)/CdS with enhanced photocatalytic activity for ketoprofen degradation: Mechanism and intermediates, *Chem. Eng. J.*, 2021, **422**, 130105, DOI: 10.1016/j.cej.2021.130105.

53 M. Murali and R. Raghunandan, Facile room temperature synthesis of ZIF-67 for efficient photocatalytic degradation of methylene blue under sunlight irradiation, *Ionics*, 2024, **30**, 4917–4930, DOI: 10.1007/s11581-024-05601-6.

54 X. Chen, J. X. Zhao, J. W. Wang, Y. Liu, L. C. Wang, R. Weerasooriya and Y. C. Wu, Doping ZIF-67 with transition metals results in bimetallic centers for electrochemical detection of Hg(II), *Electrochim. Acta*, 2021, **387**, 138539, DOI: 10.1016/j.electacta.2021.138539.

55 R. R. Ikreedeegh and M. Tahir, Indirect Z-scheme heterojunction of NH2-MIL-125(Ti) MOF/g-C3N4nanocomposite with RGO solid electron mediator for efficient photocatalytic CO2reduction to CO and CH4, *J. Environ. Chem. Eng.*, 2021, **9**, 105600, DOI: 10.1016/j.jece.2021.105600.

56 S. Sadiq, I. Khan, M. Humayun, P. Wu, A. Khan, S. Khan, A. Khan, S. Khan, A. F. Alanazi and M. Bououdina, Synthesis of Metal-Organic Framework-Based ZIF-8@ZIF-67 Nanocomposites for Antibiotic Decomposition and Antibacterial Activities, *ACS Omega*, 2023, **8**, 49244–49258, DOI: 10.1021/acsomega.3c07606.

57 M. Teranishi, S. Naya and H. Tada, In Situ Liquid Phase Synthesis of Hydrogen Peroxide from Molecular Oxygen Using Gold Nanoparticle-Loaded Titanium(IV) Dioxide Photocatalyst, *J. Am. Chem. Soc.*, 2010, **132**, 7850–7851, DOI: 10.1021/ja102651g.

58 H. Wang, F. Zhou, Z. Dai, S. Wei, Y. Wang, Y. Cao, M. Li, J. Li and J. Huang, Rational Construction of Donor-Acceptor Covalent Organic Framework Heterojunction for High-Performance Photocatalytic Production of H2O2, *Ind. Eng. Chem. Res.*, 2025, **64**, 13211–13220, DOI: 10.1021/acs.iecr.5c01807.

59 X. Wang, H. Li, S. Zhou, J. Ning, H. Wei, X. Li, S. Wang, L. Hao and D. Cao, Donor–Acceptor Fully Sp2-Carbon Conjugated Covalent Organic Frameworks for Photocatalytic H2O2 Production, *Adv. Funct. Mater.*, 2025, **30**, 2424035, DOI: 10.1002/adfm.202424035.

© 2026 The Author(s). Published by the Royal Society of Chemistry